

# Signatures of spin-orbital states of $t_{2g}^2$ system in the optical conductivity : The case of $RVO_3$ ( $R=Y$ and $La$ )

Minjae Kim<sup>1,2,\*</sup>

<sup>1</sup>*Centre de Physique Théorique, École Polytechnique,  
CNRS, Université Paris-Saclay, 91128 Palaiseau, France*

<sup>2</sup>*Collège de France, 11 place Marcelin Berthelot, 75005 Paris, France*

(Dated: September 26, 2018)

We investigate signatures of spin and orbital states of  $RVO_3$  ( $R=Y$  and  $La$ ) in the optical conductivity using density functional theory plus dynamical mean-field theory (DFT+DMFT). From the assignment of multiplet state configurations to optical transitions, the DFT+DMFT reproduces experimental temperature dependent evolutions of optical conductivity for both  $YVO_3$  and  $LaVO_3$ . We also show that the optical conductivity is a useful quantity to probe the evolution of the orbital state even in the absence of spin order. The result provides a reference to investigate spin and orbital states of  $t_{2g}^2$  vanadate systems which is an important issue for both fundamental physics on spin and orbital states and applications of vanadates by means of orbital state control.

## I. INTRODUCTION

Rare-earth vanadates,  $RVO_3$  ( $R$ =rare-earth atom), are one of the most intensively discussed materials for the nature of the interplay between the spin, orbital, and lattice degrees of freedom.<sup>1-5</sup> Understanding this coupling between the spin, orbital, and lattice degrees of freedom in  $RVO_3$  is an important fundamental problem, which has been a subject of debates regarding the origin of spin and orbital ordering, electronic superexchange versus lattice distortion. Also, this spin-orbital-lattice coupling is an important ingredient in applications of  $RVO_3$ , such as in multiferroic materials<sup>6-9</sup> and solar cells,<sup>10-12</sup> by means of heterostructure engineering. The lattice controlled spin state for  $RVO_3$  is a promising route to multiferroicity,<sup>7,9</sup> while the spin ordering driven longer lifetime of photodoped carriers for  $RVO_3$  is an important source to improve the efficiency of solar cells.<sup>11</sup>

$YVO_3$  and  $LaVO_3$  are two representative materials of the rare-earth vanadate family which exhibit different temperature ( $T$ ) dependent evolutions of the crystal structure.<sup>13,14</sup> At high  $T$ , both  $YVO_3$  and  $LaVO_3$  have orthorhombic structures of the  $Pnma$  space group with the  $a^-a^-c^+$  type Glazer rotation of octahedrons. For  $YVO_3$ , with cooling, the structural transition occurs at  $T=200$  K to the monoclinic structure of the  $P2_1/a$  space group. For lower  $T$ , below 77 K, the crystal structure of this material turns into the  $Pnma$  space group again. In contrast,  $LaVO_3$  has a larger size of the cation than that of  $YVO_3$ .<sup>13</sup> Accordingly, the  $a^-a^-c^+$  type rotation of  $LaVO_3$  is smaller than that of  $YVO_3$ . As a result, for  $LaVO_3$ , the structural transition from  $Pnma$  to  $P2_1/a$  occurs at  $T=140$  K upon cooling, and there is no structural transition below 140 K.<sup>14</sup>

The spin and orbital ordering of  $YVO_3$  and  $LaVO_3$  is related to the crystal structure for the given  $T$ . Figure 1(a) shows the electronic configuration of these materials that have two electrons in  $t_{2g}$  orbitals with the Hund's coupling induced high spin state. The  $xy$  orbital has an occupancy close to one because of its lower energy

level with respect to that of  $xz$  and  $yz$  orbitals, which is driven by the rotation and distortion of octahedron. Another electron has an orbital degrees of freedom between  $xz$  and  $yz$ . Fig.1(b and c) shows dominant Jahn-Teller distortion patterns for  $P2_1/a$  and  $Pnma$  structures.  $P2_1/a$  structure has G type Jahn-Teller distortion (JTG), and  $Pnma$  structure has C type Jahn-Teller distortion (JTC). These patterns of JT distortion lift the degeneracy on  $xz$  and  $yz$  orbitals inducing G type orbital ordering (OOG) for  $P2_1/a$  structure (JTG) and C type orbital ordering (OOC) for  $Pnma$  structure (JTC). Fig.1(f and g) shows this structure driven spin and orbital ordering pattern for OOG (antiferro OO in all axis) and OOC (ferro OO in the  $c$  axis and antiferro OO in the  $ab$  plane). With the nominal configuration in Fig.1(a), the single electron in the  $xy$  orbital induces the antiferromagnetic (AFM) superexchange interaction between nearest neighbor atoms in the  $ab$  plane. The OOG induces ferromagnetic (FM) superexchange interaction along the  $c$  axis from the Hund's coupling induced lower energy superexchange path along the  $c$  axis. And, the OOC induces AFM superexchange interaction along the  $c$  axis, because of that the ferro OO along the  $c$  axis induces the superexchange energy gain in the case of AFM order along the  $c$  axis. Accordingly, JTG ( $P2_1/a$ ) and JTC ( $Pnma$ ) distortions induce C type AFM (AFMC) and G type AFM (AFMG), respectively, in agreement with Goodenough-Kanamori-Anderson rules (GKA rules, Ref.15-17). These  $T$ -dependent spin orderings of  $YVO_3$  and  $LaVO_3$  are unambiguously determined by neutron diffraction experiments.<sup>13,18</sup>

For the explanation of experimentally confirmed spin orderings for the given  $T$ , there have been debates on orbital states for  $RVO_3$ . Due to the small crystal-field inherent to  $t_{2g}$  orbitals, the quantum orbital fluctuation of  $xz/yz$  could be relevant for the  $T$  regime of spin ordering, even in the presence of pictorial JT distortions in Fig.1(b and c). Based on this small crystal-field, the resonant valance bond (RVB) state of  $xz$  and  $yz$  orbitals is proposed as an orbital state of  $RVO_3$ .<sup>3-5</sup> In this or-

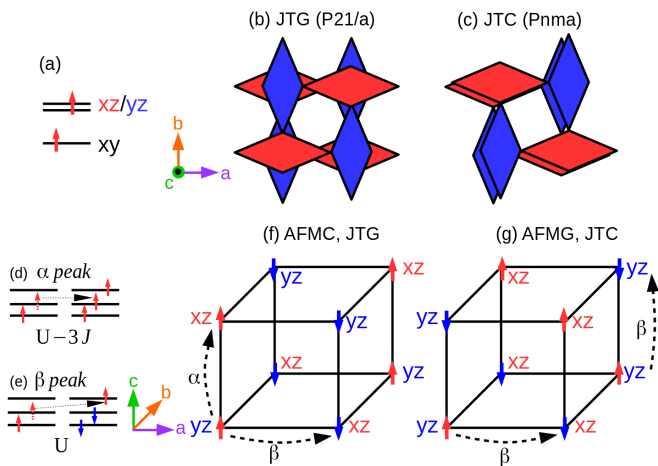


Figure 1. (Color) (a) The  $t_{2g}^2$  electron configuration in  $RVO_3$ . (b) and (c) G type Jahn-Teller distortion (JTG) in  $P2_1/a$  and C type Jahn-Teller distortion (JTC) in  $Pnma$ , respectively. Blue and red rhombus indicate distorted octahedrons. (d) and (e) Multiplet configurations of optical transitions for  $\alpha$  peak (optical gap :  $U - 3J$ ) and  $\beta$  peak (optical gap :  $U$ ) in (f) and (g) (see the text). (f) Spin-orbital configuration in the JTG and C type antiferromagnetic order (AFMC). (g) Spin-orbital configuration in the JTC and G type AFM order (AFMG).

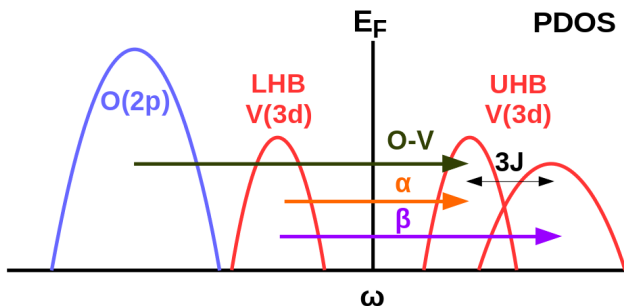


Figure 2. (Color) Schematic partial density of states (PDOS) of  $RVO_3$  and its interpretation for optical transitions,  $\alpha$ ,  $\beta$ , and O-V (O(2p) to V(3d)). LHB and UHB present lower and upper Hubbard bands, respectively. O(2p) bands contributions are also plotted.  $E_F$  indicates the Fermi level.

bitar RVB,  $xz$  and  $yz$  orbitals of nearest neighbor atoms on  $c$  axis have a singlet state, and this singlet makes the RVB along the  $c$  axis of the lattice. Accordingly, in agreement with the GKA rules, the FM superexchange interaction emerges in the  $c$  axis and AFMC emerges. In the  $P2_1/a$  structure, both the JTG and the orbital RVB induce AFMC. However, in  $LaVO_3$  at  $T \sim 150$  K, which has the  $Pnma$  structure, the JTC in the structure induces the AFMG order,<sup>18</sup> which is different from the orbital RVB induced AFMC order.<sup>3</sup> Both view points explain experiments such as the magnon spectrum of  $YVO_3$ .<sup>1,4,5</sup> But, for  $LaVO_3$ , the continuous  $T$ -dependent evolution of spin and orbital states for  $T \sim 150$  K still remains to be resolved. The fingerprint of spin-orbital states of  $LaVO_3$  in

the optical conductivity would resolve this puzzle, complementary to thermal properties such as electronic contributions to entropy.<sup>18</sup>

Optical conductivity is a powerful tool to probe phase transitions in strongly correlated systems.<sup>19</sup> Fingerprints of multiplet states of the correlated shell in the optical conductivity provide information about the spin and orbital ordering. In  $RVO_3$ , there have been issues on the explanation of  $T$ -dependent evolution of optical conductivities in experiments in terms of spin and orbital states.<sup>20-22</sup> However, there is an ambiguity in the quantitative assignment of optical peaks to multiplet states,<sup>20-22</sup> which we explain in the Sec.III A. In addition, the  $T$ -dependent evolution of optical conductivity in the theory to be compared with experiment is still lacking.

In this paper, we compute  $T$ -dependent evolutions of optical conductivity of  $RVO_3$  ( $R=Y$  and  $La$ ) using density functional theory plus dynamical mean-field theory (DFT+DMFT).<sup>23,24</sup> The approach reproduces experimental  $T$ -dependent evolutions of optical conductivity for both  $YVO_3$  and  $LaVO_3$ . We have shown that the  $T$ -dependent optical conductivity could detect spin and orbital orderings. This result could be achieved by the correct assignment of optical transitions to two peaks,  $\alpha$  and  $\beta$ , as shown in Fig.1(d and e). Furthermore, by imposing paramagnetic (PM) state for given structures of each  $T$  in the phase diagram, we have shown the orbital polarization driven evolution of optical conductivity in the absence of spin ordering. This result could be used as a reference for probing orbital states in the heterostructure of  $RVO_3$ . Also, we have shown the difference in the optical conductivity of  $LaVO_3$  at  $T \sim 150$  K in various magnetic states which would be useful for the investigation on the nature of spin and orbital states between the orbital RVB driven AFMC and the JTC driven AFMG.

## II. METHODS

We calculate the optical conductivity of  $YVO_3$  and  $LaVO_3$  within DFT+DMFT using the full potential of Ref<sup>25</sup> and the TRIQS library.<sup>26,27</sup> We compute optical conductivity using the Kubo formula with the bubble diagram of the Green's function in the DFT+DMFT.<sup>23,24</sup> We adopted experimental crystal structures of each relevant  $T$  for both  $YVO_3$  and  $LaVO_3$ .<sup>13,14</sup> For  $YVO_3$ , (i) for high  $T$  (300-500 K), the experimental crystal structure for  $T=297$  K is used ( $Pnma$ ), (ii) for intermediate  $T$  (100K), the experimental crystal structure for  $T=100$  K is used ( $P2_1/a$ ), and (iii) for low  $T$  (50K), the experimental crystal structure for  $T=65$  K is used ( $Pnma$ ).<sup>13</sup> For  $LaVO_3$ , (i) for high  $T$  (150-500 K), the experimental crystal structure for  $T=150$  K is used ( $Pnma$ ), and (ii) for low  $T$  (50-100K), the experimental crystal structure for  $T=100$  K is used ( $P2_1/a$ ).<sup>14</sup> In the DFT part of the computation, the Wien2k package was used.<sup>28</sup> The local density approximation (LDA) is used for the exchange-correlation functional. For projectors on the correlated

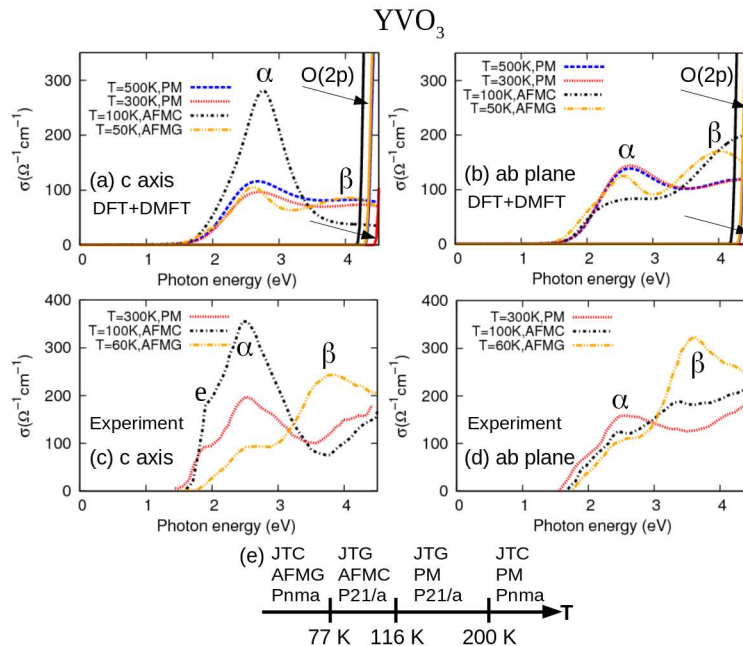


Figure 3. (Color) (a) and (b) Temperature ( $T$ ) dependent optical conductivity  $\sigma(\omega)$  of  $\text{YVO}_3$  for  $c$  axis and  $ab$  plane in DFT+DMFT. (c) and (d)  $T$ -dependent  $\sigma(\omega)$  of  $\text{YVO}_3$  for  $c$  axis and  $ab$  plane of experiment, Reul et al., Ref.20. Solid lines in (a) and (b) are for the edge of  $O(2p)$ - $V(3d)$  optical transitions for each  $T$ . The peak,  $e$ , in (c) is the exciton peak of experiment, Reul et al., Ref.20 (see the text). (e)  $T$ -dependent phase diagram of  $\text{YVO}_3$ . JTC and JTG type distortions are dominant in the  $Pnma$  and the  $P2_1/a$  structures, respectively. PM corresponds to paramagnetism.

$t_{2g}$  orbitals in DFT+DMFT, Wannier-like  $t_{2g}$  orbitals are constructed out of Kohn-Sham bands within the energy window  $[-1.1, 1.1]$  eV with respect to the Fermi energy. We use the full rotationally invariant Kanamori interaction as shown below, where  $L$  and  $S$  are angular momentum and spin momentum operators of  $t_{2g}$  orbitals,  $H_{\text{int}} = (U - 3J) \frac{N(N-1)}{2} - 2J\vec{S}^2 - \frac{J}{2}\vec{L}^2$ . (see e.g. the algebra in Ref.29) For  $U$  and  $J$  parameters of the Kanamori interaction, we used  $U=4.5$  eV and  $J=0.5$  eV. This parameter range is shown in Ref.2 to be relevant for the description of experimental photoemission spectrum (Ref.30 and 31) of  $\text{YVO}_3$  and  $\text{LaVO}_3$  from the  $t_{2g}$  low energy effective model of the DFT+DMFT.<sup>32</sup> One thing should be noticed is that in Ref.2, only the density-density type interaction in the Kanamori interaction is used. Using the full rotationally invariant Kanamori interaction including the spin-flip and the pair-hopping terms is essential to describe the correct splitting of  $\alpha$  and  $\beta$  peaks in the optical conductivity which have different multiplets in optical transitions as shown in Fig.1(d and e). To solve the quantum impurity problem in the DMFT, we used the strong-coupling continuous-time Monte Carlo impurity solver<sup>33</sup> as implemented in the TRIQS library.<sup>26,34</sup>

### III. RESULTS

In this section, we present our results for the optical conductivity of  $\text{YVO}_3$  and  $\text{LaVO}_3$ . In Sec.III A, we assigned main features of optical conductivity,  $\alpha$ ,  $\beta$ , and  $O(2p)$ - $V(3d)$  peaks, to the multiplet of final states of optical transitions, and also discussed their relation to magnetic states. In Sec.III B, we presented the  $T$ -dependent evolution of optical conductivity and compared the result with experiments. In Sec.III C, we presented the  $T$ -dependent the evolution of orbital states in the  $xz$ ,  $yz$ , and  $xy$  states. This  $T$ -dependent orbital state is also computed by imposing PM state. Under this PM state, the  $T$ -dependent optical conductivity is discussed. In Sec.III D, we presented evolution optical conductivity of  $\text{LaVO}_3$  as function of  $T$  around 150K for various spin states, and suggest possible fingerprints of the spin state in the optical conductivity for this  $T$  regime.

#### A. Multiplet states and optical conductivity

Two main peaks,  $\alpha$  and  $\beta$ , in the optical conductivity can be assigned to the optical transitions having multiplet configurations in Figure1(d and e). The  $\alpha$  peak corresponds to the inter-site electron transfer within the FM spin states, and the  $\beta$  peak corresponds to the inter-site electron transfer within the AFM spin states. Figure2 presents schematic partial density of states (PDOS)

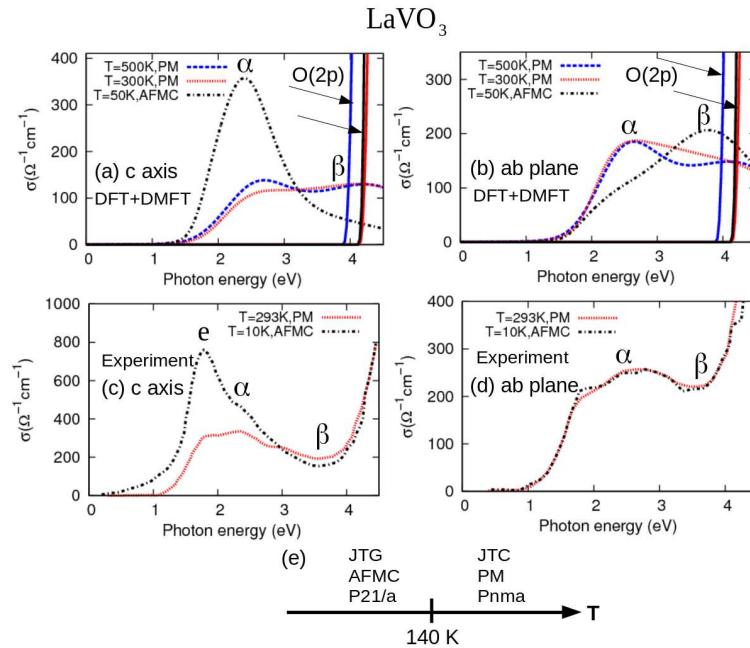


Figure 4. (Color) (a) and (b)  $T$ -dependent  $\sigma(\omega)$  of  $\text{LaVO}_3$  for  $c$  axis and  $ab$  plane in DFT+DMFT. (c) and (d)  $T$ -dependent  $\sigma(\omega)$  of  $\text{LaVO}_3$  for  $c$  axis and  $ab$  plane of experiment, Miyasaka et al., Ref.21. Solid lines in (a) and (b) are for the edge of  $\text{O}(2p)$ - $\text{V}(3d)$  optical transitions for each  $T$ . The peak  $e$  in the experiment, in (c) is interpreted as an exciton peak (see the text). (e)  $T$ -dependent phase diagram of  $\text{LaVO}_3$ .

of  $\text{O}(2p)$  and  $\text{V}(3d)$  bands and its interpretation for the optical transitions,  $\alpha$ ,  $\beta$ , and  $\text{O}(2p)$ - $\text{V}(3d)$ . Photon energies for  $\alpha$  and  $\beta$  peaks are  $U - 3J$  and  $U$ , respectively. Due to the incomplete orbital polarization of  $xz/yz$  and the rotation of octahedron which breaks cubic symmetry, the inter-orbital optical transition is also possible. The spectral weight from the optical transition, which has a double occupancy in the same orbital for the final state, has the corresponding photon energy of  $U + 2J$ . This spectral weight is buried in  $\text{V}(3d)$ - $\text{O}(2p)$  optical transition as shown in Fig.2. Fig.3 shows that the peak position of  $\alpha$  and  $\beta$  in our DFT+DMFT results (Fig.3 a and b) is consistent with experiments (Fig.3 c and d) of Ref.20. The splitting between  $\alpha$  and  $\beta$  peaks,  $3J$  ( $\sim 1.5$  eV), in DFT+DMFT results is consistent with experiments. This result indicates that the above description of  $\alpha$  and  $\beta$  peaks is correct.

### B. Temperature dependent evolution of optical conductivity

Figure 3 presents the  $T$ -dependent evolution of the optical conductivity of  $\text{YVO}_3$ . From the change of  $T$  from 500 K to 300 K, in the DFT+DMFT result, it is shown that there are little changes in the optical conductivity in both  $ab$  plane and  $c$  axis. In this  $T$  range, the crystal structure is  $Pnma$  and the spin state is PM. From the change of  $T$  from 300 K to 100 K, there is a structural transition from  $Pnma$  to  $P2_1/a$ , and accordingly, there

is an onset of the AFMC ordering which is related to the transition of octahedron distortion from JTC to JTG. As shown in Fig.1(f), this AFMC ordering induces an enhancement (suppression) of  $\alpha$  ( $\beta$ ) peak for  $c$  axis and the opposite trend for  $ab$  plane. In Fig.3, it is shown that the DFT+DMFT result is remarkably consistent with experiment.<sup>20</sup> With the change of  $T$ , from 100 K to  $\sim 50$  K, there is a structural transition from  $P2_1/a$  to  $Pnma$  with the onset of the AFMG ordering and the transition of distortion from JTG to JTC. In this state, all inter-site spin configurations are AFM as shown in Fig1(g). As a result, the optical conductivity becomes more isotropic, with a suppression of  $\alpha$  peak and an enhancement of  $\beta$  peak for both  $c$  axis and  $ab$  plane, with respect to PM state. This result in DFT+DMFT for 100 K to  $\sim 50$  K is consistent with the experiment.<sup>20</sup> The overall evolution of  $\alpha$  peak heights in  $c$  axis in the present DFT+DMFT result, ( $97$ ,  $281$ , and  $105 \text{ } \Omega^{-1}\text{cm}^{-1}$  for  $300$ ,  $100$ , and  $50$  K, respectively) is consistent with the experiment ( $198$ ,  $355$ , and  $92 \text{ } \Omega^{-1}\text{cm}^{-1}$  for  $300$ ,  $100$ , and  $60$  K, respectively).<sup>20</sup> In the photon energy above 4 eV, the optical transition of  $\text{O}(2p)$ - $\text{V}(3d)$  is activated. As a result, as shown in Fig.3, there is an upturn of optical conductivities, and the  $\beta$  peak is partially buried, consistent with experiments.<sup>20</sup>

There are several features in the experimental optical conductivity which are not resolved in our DFT+DMFT computation. There is a sub-peak,  $e$ , below the  $\alpha$  peak in the experiment (Fig.3(c)). This peak is the exciton below the band gap as shown in Ref.20. The non-equilibrium evolution of the  $e$  peak and the  $\alpha$  peak in the pump probe



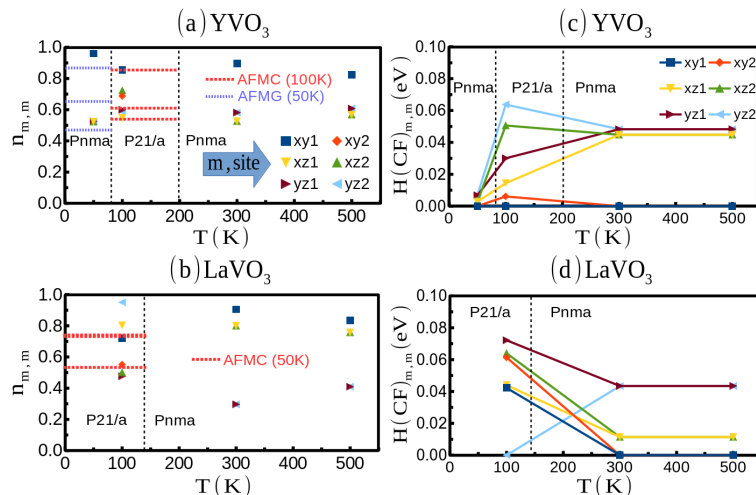


Figure 5. (Color) (a) and (b)  $T$ -dependent orbital density of YVO<sub>3</sub> and LaVO<sub>3</sub>, respectively. In the case of the  $P2_1/a$  space group, two sites, 1 and 2, are symmetrically non-equivalent. Dots are orbital densities in the PM states. Red (dashed) and blue (dotted) lines are orbital densities in the AFMC and AFMG states in Fig.3 and Fig.4, which are averaged per site. The deviation from the averaged value in AFM states is less than 0.077. (c) and (d)  $T$  dependent evolution of crystal-field for YVO<sub>3</sub> and LaVO<sub>3</sub>, respectively, for crystal structures used in the present DFT+DMFT computation.<sup>13,14</sup> The lowest crystal-field energy level is set as a zero energy for each structures.

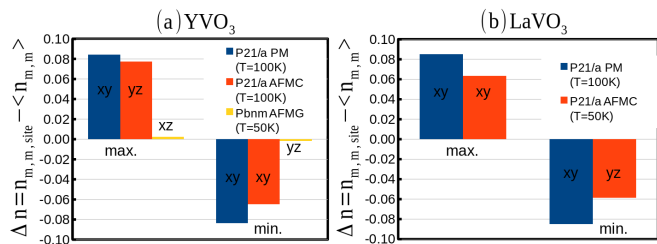


Figure 6. (Color) (a) The maximum and the minimum of orbital density deviations within all non-equivalent site from the site averaged orbital density, for each spin state for YVO<sub>3</sub>. Orbital which has the maximum or the minimum are presented for each cases. (b) Same as (a) for LaVO<sub>3</sub>. It is shown that the onset of magnetism results in the reduction of the deviation for both YVO<sub>3</sub> and LaVO<sub>3</sub> for  $P2_1/a$  structure.

experiment of YVO<sub>3</sub> in Ref.35 shows that this subpeak below the  $\alpha$  is indeed the exciton below the band gap. This assignment of peaks is different from previous reports in RVO<sub>3</sub> of Ref.21 and 22, which argue that the  $e$  and the  $\alpha$  peaks in our viewpoint are  $\alpha$  and  $\beta$  peaks in Fig.1(d and e) and Fig.2, respectively. This is the reason why previous optical conductivity data from DFT is different from experiments.<sup>22</sup> The emergence of the  $e$  peak is from the condensation of the exciton below the band gap which is induced by non-local correlations, interpreted as a condensation of the charge carrier state along the ferromagnetic chain in the AFMC state.<sup>20</sup> Present DFT+DMFT computation includes local dynamical electronic correlations by the non-perturbative manner and spatial static electronic correlations from the exchange-correlation functional in the LDA. As a result, the  $e$

peak from the non-local correlation is not described in the present results.

Figure 4 presents the  $T$ -dependent evolution of optical conductivity for LaVO<sub>3</sub>. For  $T$  range from 500 K to 300 K, in the DFT+DMFT result, it is shown that there is a small change in the optical conductivity in both  $ab$  plane and  $c$  axis, similar to the case of YVO<sub>3</sub>. With changes of  $T$  from 300 K to 50 K, the structural transition from  $Pnma$  to  $P2_1/a$  occurs. Accordingly, there is an onset of the AFMC ordering which is related to the transition from JTC to JTG. Similar to the case of YVO<sub>3</sub> for 300 K to 100 K, this AFMC ordering induces an enhancement of  $\alpha$  peak heights for  $c$  axis and the opposite trend in the  $ab$  plane. As shown in Fig.4, the DFT+DMFT result for 300 K to 50 K is consistent with the experiment for  $c$  axis.<sup>21</sup> We suggest that the  $e$  peak in Fig.4(c) is the exciton peak similar to the YVO<sub>3</sub>. For the optical conductivity of  $ab$  plane, differently from the DFT+DMFT result, there is a small evolution of optical conductivity in the experiment, which is remained to be resolved.<sup>21</sup> The overall evolution of  $\alpha$  peak heights in  $c$  axis in the present DFT+DMFT result, (120, and 357  $\Omega^{-1}cm^{-1}$  for 300, and 50 K, respectively) is consistent with the experiment (330, and 570  $\Omega^{-1}cm^{-1}$  for 293, and 10 K, respectively).<sup>21</sup>

There are two important differences in the optical conductivity for YVO<sub>3</sub> and LaVO<sub>3</sub>. Firstly, due to the smaller rotation of the octahedron in LaVO<sub>3</sub>, which give rise to the enhanced  $O(2p)$ - $V(3d)$  hybridization, the optical transition of  $O(2p)$ - $V(3d)$  is activated at the lower photon energy (around 4 eV) in LaVO<sub>3</sub> with respect to that in YVO<sub>3</sub> (above 4 eV). As a result, as shown in Fig.4, the  $\beta$  peak center is buried from the  $O(2p)$ - $V(3d)$  peak in LaVO<sub>3</sub>, consistent with experiments.<sup>21</sup> This difference

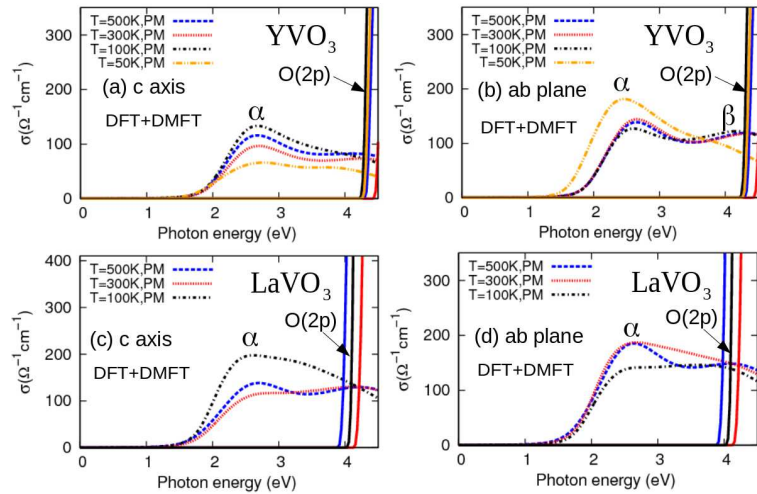


Figure 7. (Color) (a) and (b)  $T$ -dependent  $\sigma(\omega)$  of  $\text{YVO}_3$  for  $c$  axis and  $ab$  plane in DFT+DMFT with the constraint of PM state. (c) and (d)  $T$ -dependent  $\sigma(\omega)$  of  $\text{LaVO}_3$  for  $c$  axis and  $ab$  plane in DFT+DMFT with the constraint of PM state. Solid lines are for the edge of  $\text{O}(2p)$ - $\text{V}(3d)$  optical transitions.

of the energy of the  $\text{O}(2p)$ - $\text{V}(3d)$  transition explains the presence of the  $T$  dependent evolution of the  $\beta$  peak in  $\text{YVO}_3$  and the absence of the  $T$  dependent evolution of the  $\beta$  peak in  $\text{LaVO}_3$ .<sup>20,21</sup> Therefore, we suggest to analyse (i)  $T$ -dependent evolution of the  $\alpha$  peak to resolve spin-orbital structure in the case of bulk  $\text{LaVO}_3$  and (ii) the appearance of the  $\beta$  peak in the heterostructure of  $\text{LaVO}_3$  in the case of compressive strain to confirm the reduced  $\text{O}(2p)$ - $\text{V}(3d)$  hybridization from the enhanced rotation of octahedron. Secondly, there is a difference in the height of the  $e$  peaks. The height of  $e$  peaks are  $179$  and  $760 \text{ } \Omega^{-1} \text{cm}^{-1}$  for  $\text{YVO}_3$  and  $\text{LaVO}_3$ , respectively. We suggest that this larger height of the  $e$  peak in  $\text{LaVO}_3$  is due to the smaller octahedron rotation which results in the larger stabilization of the kinetic energy of the exciton for  $\text{LaVO}_3$ .

### C. Orbital states dependence of optical conductivity

Figure 5 presents the  $T$ -dependent evolution of orbital density and crystal-field of  $xz$ ,  $yz$ , and  $xy$  orbital in the  $t_{2g}$  manifold for  $\text{YVO}_3$  and  $\text{LaVO}_3$ . None of orbitals are fully polarized due to the low symmetry crystal-field contribution from the rotation of the octahedrons and the covalent bonding with cations.<sup>2</sup>

For  $T$  range of 300-500 K, in Fig.5(a) and 5(b), there is a small evolution of orbital polarization which is consistent with Ref.2 This result explains the small evolution of the optical conductivity in the  $T$  range of 300-500 K, as shown in Fig.3 and 4. Fig.5(c) and (d) shows  $T$  dependent crystal-field levels in the crystal structures used in present results. The  $Pnma$  structure has a single type of crystal-field level for all sub-lattice of V (site-uniform), and the  $P2_1/a$  structure has two types of crystal-field

level for sub-lattice of V (site-non-uniform). In the PM state of this  $T$  range, the site-uniform crystal-field splitting, is not effective to induce the  $T$ -dependent evolution of orbital polarization.

Figure 6 shows that in the AFMC state, the orbital polarization of  $xz$  and  $yz$  is more uniform than that of the PM state for  $P2_1/a$  structure. Also, as shown in Fig.5(a), especially for the  $Pnma$  structure of  $\text{YVO}_3$  for  $T=50$  K, the orbital polarization in the AFMG state is much larger than that of the PM state. These results suggest that JT distortions from the structural transition induce a finite orbital polarization, and the superexchange interaction modifies this orbital polarization with the onset of AFM spin ordering. The size of the induced magnetic moment for each site is  $1.97 \mu_B$  for AFMG state. This large magnetic moment induced exchange field to orbitals results in the large orbital polarization in the AFMG state with respect to that in the PM state as shown in Fig.5(a). This result shows that both JT distortion and superexchange interaction contribute to the orbital polarization. This result is in line with the inelastic x-ray scattering experiment on  $\text{YVO}_3$  which shows that the orbital excitation has contributions from both superexchange and crystal-field.<sup>36</sup>

Fig. 6 shows the maximum and the minimum of orbital density deviations within all site from the site averaged orbital density, for each spin states, for  $\text{YVO}_3$  and  $\text{LaVO}_3$ . It is shown that the onset of magnetic ordering results in the reduction of the site dependence of the orbital polarization in both  $\text{YVO}_3$  (Fig.6(a)) and  $\text{LaVO}_3$  (Fig.6(b)). As shown in Fig.5(c) and (d), the crystal-field in the structure of  $P2_1/a$  space group is non-uniform for sites. On the other hand, the magnetic moment for magnetic states of all case is uniform for sites. The site dependent deviation of magnetic moment size is smaller than  $0.01 \mu_B$ . As a result, the site-uniform orbital polar-

ization from the site-uniform spin exchange interaction is induced in all AFM state. This site-uniform orbital state in AFM states is different from the crystal-field driven site-non-uniform orbital polarization, which is induced for PM states of the  $P2_1/a$  space group.

In  $P2_1/a$  structures for  $YVO_3$  and  $LaVO_3$ , the orbital polarization for  $xz$  and  $yz$  is larger in the case of  $LaVO_3$  for PM spin state. This result is due to the nature of the JT distortion in the  $P2_1/a$  structure. In Ref.9, it was shown that both JTC and JTG distortions exist for  $P2_1/a$  structures of  $YVO_3$  and  $LaVO_3$ . In the case of  $LaVO_3$ , JTG type distortion is much larger than JTC type distortion. On the one hand,  $YVO_3$  has also larger JTG type distortion than that of JTC, but the difference is smaller than that of  $LaVO_3$ .<sup>9</sup> As a result, the orbital polarization is larger for  $LaVO_3$  with respect to that of  $YVO_3$  for  $P2_1/a$  structure in PM state, consistent with Ref.2, as shown in Fig.5(a and b).

Figure 7 presents the  $T$ -dependent evolution of optical conductivity in DFT+DMFT with the constraint of PM state. With the constraint of PM state, Kramers doublet, spin up and spin down components, are set to equal, and orbital differentiation is allowed with constraint from the given symmetry of crystal structure. Even in the constraint of PM, due to the superexchange energy gain according to the GKA rules, antiferro OO and ferro OO enhances FM ( $\alpha$  peak) and AFM ( $\beta$  peak) spin correlations, respectively. As a result, the orbital polarization in the PM state also contributes to the evolution of optical conductivity. For the structural transition from the  $Pnma$  to the  $P2_1/a$ , 300K to 100K of  $T$ ,  $LaVO_3$  shows a large evolution of optical conductivity, while  $YVO_3$  shows a small variation. The larger JTG type orbital polarization in the  $P2_1/a$  structure of  $LaVO_3$  induces the AFMC type spin correlation. On the other hand, the optical conductivity of  $YVO_3$  for  $P2_1/a$  structure shows small variations because of the small difference in the magnitude of JTG and JTC type distortions. Thus, the trend, such that  $\alpha$  ( $\beta$ ) peak is much enhanced (suppressed) for  $c$  axis and the opposite change occurs for  $ab$  plane, is larger for  $LaVO_3$ . This trend is consistent with the larger orbital polarization in  $LaVO_3$  with respect to that in  $YVO_3$  for  $P2_1/a$  structures in PM state as shown in Fig.5 (a) and (b).

For  $YVO_3$ , in Fig.5(a), it is shown that in the  $Pnma$  structure of  $T=50K$  for PM state, the orbital occupancy of the  $xy$  orbital is close to 1. And also, there is unquenched orbital fluctuation of  $xz$  and  $yz$  for the PM state. This result provides an explanation of the optical conductivities of  $T=50K$  for PM state in Fig.7(a and b). With the constraint of ferro OO in  $c$  axis (OOC) from the JTC distortion of  $Pnma$  structure, the orbital state of  $xz$  and  $yz$  in the apical direction has same phase. As a result, there is a strong suppression of optical transition for  $c$  axis due to the blocking of the charge transfer for  $c$  axis. On the other hand, the orbital fluctuation of  $xz$  and  $yz$  is in different phase for  $ab$  plane due to the symmetry of  $Pnma$ , which enhances in-plane FM correlation. As

a result, the height of  $\alpha$  peak is enhanced for  $ab$  plane. These results suggest that the optical conductivity is a useful quantity to probe the orbital state of  $RVO_3$ , which is complimentary to the resonant x-ray diffraction experiment. We suggest to compare heights of the  $\alpha$  peak for consistent analysis of spin-orbital states from optical conductivity of  $RVO_3$  systems, because, in the case of  $LaVO_3$ , the  $\beta$  peak is buried in the  $O(2p)$ - $V(3d)$  peak.

#### D. Spin state and optical conductivity of $LaVO_3$ for $T_{str} < T < T_N$ ( $T \sim 150K$ )

Figure 8 presents  $T$ -dependent evolution of optical conductivity of  $LaVO_3$  in the DFT+DMFT computation at the  $T$  above the structural transition ( $T_{str}$ ) and below the  $T$  for the spin ordering ( $T_N$ ), which corresponds to  $T \sim 150$  K. At this  $T$ , there is a debate on the spin ordering.<sup>3,18</sup> The structural distortion of JTC in the  $Pnma$  space group above  $T_{str}$  induces the AFMG ordering. On the other hand, the superexchange driven orbital RVB state induces AFMC. We compute the optical conductivity of AFMG and PM states at 150 K in the structure of the  $Pnma$  space group. For this  $T$ , the AFMC state is not stabilized, which implies that the description of the free energy in the present level of approximation in the DFT+DMFT does not have a local minimum for the AFMC state for the structure of  $T=150$  K. The result is compared with results for the AFMC state at 100 K ( $P2_1/a$  structure) and the PM state at 300 K ( $Pnma$  structure). It is clearly shown that in the case that the AFMG ordering emerges for  $T_{str} < T < T_N$ , the  $\alpha$  peak is suppressed for  $c$  axis with respect to the case for the AFMC state. This trend from the AFMG state is apparently different from the anisotropic optical conductivity for the AFMC state. We suggest that the measurement of the evolution of optical conductivity in the regime of  $T_{str} < T < T_N$  would be useful for resolving the issue on spin ordering between the JTC structure driven AFMG

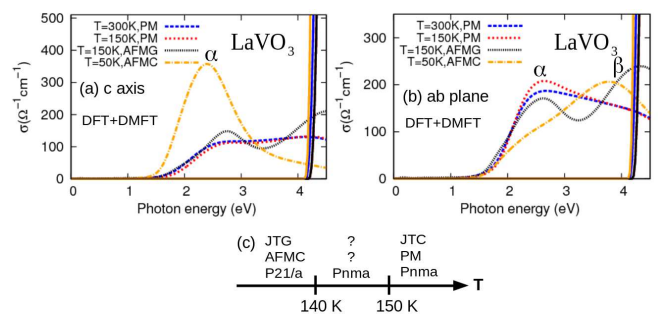


Figure 8. (Color) (a) and (b)  $T$ -dependent  $\sigma(\omega)$  of  $LaVO_3$  for  $c$  axis and  $ab$  plane in DFT+DMFT including  $\sigma(\omega)$  at  $T=150$  K ( $Pnma$  space group) for PM and AFMG states. The AFMC state is not stabilized at  $T=150$  K. (c)  $T$ -dependent phase diagram of  $LaVO_3$  around 150 K. Solid lines are for the edge of  $O(2p)$ - $V(3d)$  optical transitions.

and the electronic superexchange induced orbital RVB driven AFMC.

#### IV. DISCUSSION

We have shown that the  $T$ -dependent evolution of optical conductivity of  $YVO_3$  and  $LaVO_3$  has signatures of spin and orbital states in these materials. DFT+DMFT reproduces experimental results from the correct assignment of multiplet states to peaks in the optical conductivity. Two types of magnetic state, AFMG and AFMC, could be resolved by the optical conductivity. Furthermore, we have shown that there is a fingerprint of the  $T$ -dependent evolution of the orbital polarization in the optical conductivity even in the absence of the spin or-

der. This result provides a reference to probe orbital states in the heterostructure of  $RVO_3$ .<sup>37,38</sup> The clear difference between AFMG and AFMC states indicates that the optical conductivity is useful for resolving issues on the spin ordering of  $LaVO_3$  for the regime of  $T_{str} < T < T_N$ , which depends on its origin between the electronic superexchange induced orbital RVB and the JT crystal-field induced OO.

#### ACKNOWLEDGMENTS

We acknowledge useful discussions with Antoine Georges, Stefano Gariglio, Hugo Meley, and Alaska Subedi. This work was supported by the European Research Council (ERC-319286 QMAC), and by the Swiss National Science Foundation (NCCR MARVEL).

---

\* garix.minjae.kim@gmail.com

- <sup>1</sup> Z. Fang and N. Nagaosa, Physical review letters **93**, 176404 (2004).
- <sup>2</sup> M. De Raychaudhury, E. Pavarini, and O. Andersen, Physical review letters **99**, 126402 (2007).
- <sup>3</sup> G. Khaliullin, Progress of Theoretical Physics Supplement **160**, 155 (2005).
- <sup>4</sup> P. Horsch, G. Khaliullin, and A. M. Oleś, Physical review letters **91**, 257203 (2003).
- <sup>5</sup> C. Ulrich, G. Khaliullin, J. Sirker, M. Reehuis, M. Ohl, S. Miyasaka, Y. Tokura, and B. Keimer, Physical review letters **91**, 257202 (2003).
- <sup>6</sup> Y. Hotta, T. Susaki, and H. Hwang, Physical review letters **99**, 236805 (2007).
- <sup>7</sup> G. Jackeli and G. Khaliullin, Physical review letters **101**, 216804 (2008).
- <sup>8</sup> S. Y. Park, A. Kumar, and K. M. Rabe, Physical Review Letters **118**, 087602 (2017).
- <sup>9</sup> J. Varignon, N. C. Bristowe, E. Bousquet, and P. Ghosez, Scientific reports **5**, 15364 (2015).
- <sup>10</sup> E. Assmann, P. Blaha, R. Laskowski, K. Held, S. Okamoto, and G. Sangiovanni, Physical review letters **110**, 078701 (2013).
- <sup>11</sup> M. Eckstein and P. Werner, Physical review letters **113**, 076405 (2014).
- <sup>12</sup> L. Wang, Y. Li, A. Bera, C. Ma, F. Jin, K. Yuan, W. Yin, A. David, W. Chen, W. Wu, *et al.*, Physical Review Applied **3**, 064015 (2015).
- <sup>13</sup> G. Blake, T. Palstra, Y. Ren, A. Nugroho, and A. Menovsky, Physical Review B **65**, 174112 (2002).
- <sup>14</sup> P. Bordet, C. Chaillout, M. Marezio, Q. Huang, A. Santoro, S. Cheong, H. Takagi, C. Oglesby, and B. Batlogg, Journal of Solid State Chemistry **106**, 253 (1993).
- <sup>15</sup> J. Kanamori, Journal of Physics and Chemistry of Solids **10**, 87 (1959).
- <sup>16</sup> J. B. Goodenough, Physical Review **100**, 564 (1955).
- <sup>17</sup> P. Anderson, Physical Review **79**, 350 (1950).
- <sup>18</sup> J.-S. Zhou, Y. Ren, J.-Q. Yan, J. Mitchell, and J. Goodenough, Physical review letters **100**, 046401 (2008).
- <sup>19</sup> D. N. Basov, R. D. Averitt, D. Van Der Marel, M. Dressel, and K. Haule, Reviews of Modern Physics **83**, 471 (2011).

- <sup>20</sup> J. Reul, A. Nugroho, T. Palstra, and M. Grüninger, Physical Review B **86**, 125128 (2012).
- <sup>21</sup> S. Miyasaka, Y. Okimoto, and Y. Tokura, Journal of the Physical Society of Japan **71**, 2086 (2002).
- <sup>22</sup> Z. Fang, N. Nagaosa, and K. Terakura, Physical Review B **67**, 035101 (2003).
- <sup>23</sup> A. Georges, G. Kotliar, W. Krauth, and M. J. Rozenberg, Rev. Mod. Phys. **68**, 13 (1996).
- <sup>24</sup> G. Kotliar, S. Y. Savrasov, K. Haule, V. S. Oudovenko, O. Parcollet, and C. Marianetti, Reviews of Modern Physics **78**, 865 (2006).
- <sup>25</sup> M. Aichhorn, L. Pourovskii, V. Vildosola, M. Ferrero, O. Parcollet, T. Miyake, A. Georges, and S. Biermann, Physical Review B **80**, 085101 (2009).
- <sup>26</sup> O. Parcollet, M. Ferrero, T. Ayrál, H. Hafermann, I. Krivenko, L. Messio, and P. Seth, Computer Physics Communications **196**, 398 (2015).
- <sup>27</sup> M. Aichhorn, L. Pourovskii, P. Seth, V. Vildosola, M. Zingl, O. E. Peil, X. Deng, J. Mravlje, G. J. Kraberger, C. Martins, *et al.*, Computer Physics Communications **204**, 200 (2016).
- <sup>28</sup> P. Blaha, K. Schwarz, G. Madsen, D. Kvasnicka, and J. Luitz, An augmented plane wave+ local orbitals program for calculating crystal properties (2001).
- <sup>29</sup> A. Georges, L. de' Medici, and J. Mravlje, Annual Reviews of Condensed Matter Physics **4**, 137 (2013), <http://arxiv.org/abs/1207.3033>.
- <sup>30</sup> H. Pen, M. Abbate, A. Fujimori, Y. Tokura, H. Eisaki, S. Uchida, and G. Sawatzky, Physical Review B **59**, 7422 (1999).
- <sup>31</sup> K. Maiti and D. Sarma, Physical Review B **61**, 2525 (2000).
- <sup>32</sup> M. Casula, P. Werner, L. Vaugier, F. Aryasetiawan, T. Miyake, A. Millis, and S. Biermann, Physical review letters **109**, 126408 (2012).
- <sup>33</sup> E. Gull, A. J. Millis, A. I. Lichtenstein, A. N. Rubtsov, M. Troyer, and P. Werner, Rev. Mod. Phys. **83**, 349 (2011).
- <sup>34</sup> P. Seth, I. Krivenko, M. Ferrero, and O. Parcollet, Computer Physics Communications **200**, 274 (2016).



- <sup>35</sup> F. Novelli, D. Fausti, J. Reul, F. Cilento, P. H. van Loosdrecht, A. A. Nugroho, T. T. Palstra, M. Grüninger, and F. Parmigiani, *Physical Review B* **86**, 165135 (2012).
- <sup>36</sup> E. Benckiser, L. Fels, G. Ghiringhelli, M. M. Sala, T. Schmitt, J. Schlappa, V. Strocov, N. Mufti, G. Blake, A. Nugroho, *et al.*, *Physical Review B* **88**, 205115 (2013).
- <sup>37</sup> H. Weng and K. Terakura, *Physical Review B* **82**, 115105 (2010).
- <sup>38</sup> G. Sclauzero and C. Ederer, *Physical Review B* **92**, 235112 (2015).